buildings

MDPI

Article

Expansive Agent-Modified Geopolymer for Medium-to-Wide Concrete Crack Remediation: Workability, Mechanical Performance, and Durability

Yinghao Chen [1], Zhiyuan Lu [2,*], Linghai Kong [3], Genfu Liang [3], Jianxin Yin [4], Sheng Li [5], Guan Wu [5], Junhao Xie [1] and Zhengdong Luo [1]

[1] College of Civil Engineering, Xiangtan University, Xiangtan 411105, China
[2] School of Management Engineering, Yunnan Water Resources and Hydropower Vocational College, Kunming 650202, China
[3] The Third Engineering Co., Ltd. of CCCC Third Highway Engineering Bureau, Wuhan 430030, China
[4] CAMCE Engineering Co., Ltd., Beijing 100080, China
[5] Yueyang Transportation Quality and Safety Supervision Station, Yueyang 414000, China
* Correspondence: lzy_slsdzy@163.com

Abstract

The inherent drying shrinkage of geopolymers restricts their widespread application in concrete crack repair, particularly for medium-to-wide cracks that demand stringent workability and penetrability. This study systematically investigates the effects of three single-component expansive agents (MgO, CaO, and CSA) on the fresh properties, mechanical performance, and microstructural evolution of a slag-fly ash-based geopolymer. The optimal modified formulation was subsequently evaluated for remediating preinduced concrete cracks (2.0, 2.5 and 3.0 mm apertures) and benchmarked against ordinary Portland cement and epoxy resin. The results indicate that while CaO and CSA severely compromise paste fluidity and induce rapid setting, MgO modification provides an exceptional operational window. An 8 wt.% MgO dosage (MG8) induces only a marginal 3.73% reduction in paste fluidity and maintains stable initial and final setting times, thereby preserving excellent workability retention and enabling precise construction scheduling. Microstructural analyses (XRD, SEM, and MIP) reveal that the precipitation of micro expansive $Mg(OH)_2$ effectively suppresses the 28-day drying shrinkage to 0.23%, while facilitating the attainment of a robust compressive strength of 44.1 MPa and preserving a highly favorable strength development trajectory. In the structural repair phase, the MG8 demonstrated outstanding compressive strength recovery, peaking at 28.80 MPa for 2.0 mm cracks, which significantly outperformed both the cement and epoxy resin repaired groups. Conversely, the epoxy resin repaired specimens exhibited superior splitting tensile strength due to the inherent elongation properties of the flexible macromolecular polymer. Comprehensive durability assessments revealed that the MG8 repair system exhibits exceptional resistance against freeze–thaw cycles and sulfate/chloride attacks, ensuring long-term structural integrity that significantly outperforms conventional materials. Overall, this work presents a viable and durable geopolymer-based alternative to traditional materials, aiming to ensure timely and reliable remediation concrete cracks that do not cause structural damage.

Keywords: expansive agent; geopolymer; workability; crack repair; concrete substrate; durability

Check for updates

Academic Editor: Geo Paul

Received: 1 April 2026
Revised: 22 April 2026
Accepted: 24 April 2026
Published: 27 April 2026

Copyright: © 2026 by the authors. Licensee MDPI, Basel, Switzerland. This article is an open access article distributed under the terms and conditions of the Creative Commons Attribution (CC BY) license.

1. Introduction

Concrete is recognized as the dominant material in contemporary construction due to its cost-effectiveness, robustness, the ability to design any geometry and excellent compatibility with steel reinforcement [1,2]. Concrete structures which serve in complex geological environments, such as mine shafts and tunnel linings, inevitably suffer from progressive damage and micro-crack development due to material degradation, environmental erosion, and cyclic loading [3,4]. These cracks act as rapid diffusion channels for aggressive media, accelerating matrix deterioration and reinforcement corrosion [5], thereby severely compromising structural safety and service life, and increasing the risk of collapse, with potentially severe casualties and substantial economic losses [6,7]. Grouting is widely recognized as the mainstream technique for crack rehabilitation [8]. Currently, ordinary Portland cement (OPC) and organic polymers like epoxy resin are predominantly used [9,10]. However, OPC grout suffers from slow setting times, high shrinkage leading to secondary cracking, and massive carbon emissions during its production [11]. Conversely, while epoxy resin cures rapidly and exhibits high bond strength, its thermal expansion coefficient significantly mismatches that of concrete, rendering it prone to interfacial debonding under temperature fluctuations [12]. Furthermore, epoxy resin poses environmental and health risks [13]. Therefore, developing a rapid-hardening, highly durable, and low-carbon alternative is imperative for sustainable infrastructure maintenance.

Geopolymer is synthesized via alkali activation of industrial solid wastes rich in reactive aluminosilicates and has emerged as a highly promising low-carbon cementitious binder [14,15]. Characterized by outstanding mechanical performance and exceptional resistance to acidic and alkaline attack [16,17], it exhibits significant potential as a sustainable alternative to cement for concrete crack repair. Compared with epoxy resin, whose interfacial bond can deteriorate markedly when the temperature approaches the glass-transition range, geopolymer repair materials are inorganic and can maintain more stable bonding with cementitious substrates at elevated temperatures [18]. Moreover, at the concrete scale, the reported coefficient of the thermal expansion of fly ash-slag geopolymer concrete is close to that of ordinary Portland cement concrete, which is beneficial for thermal compatibility between the repair system and the substrate [19]. Nevertheless, the inherent shrinkage of geopolymer restricts its widespread engineering application [20,21]. Incorporating expansive agents serves as a highly effective and immediate mitigation strategy [22]. Experimental investigations by He et al. [23] demonstrated that calcium-rich additives can effectively decelerate the shrinkage rate of alkali-activated slag. Similarly, Jia et al. [24] proposed the use of calcium sulfoaluminate (CSA) and calcium oxide (CaO) to mitigate the shrinkage of slag-based geopolymers, reporting that the 56-day drying shrinkage of the modified pastes was reduced by 41–45% and 54–56%, respectively. Furthermore, Panchmatia et al. [25] discovered that zinc-based expansive agents are particularly efficacious in alleviating the shrinkage of geopolymer pastes under elevated temperature conditions.

Exploratory work regarding the engineering application of geopolymers is also underway. For instance, in pavement repair, Phoo-Ngernkham et al. [26] used high-calcium fly ash-based geopolymer to partially replace ordinary Portland cement in preparing a composite repair material, and demonstrated that its interfacial shear strength is significantly higher than that of commercially available pavement repair materials. Zhang et al. [27] reported that high-calcium fly ash-based geopolymers modified with MgO and a combined expansive agent successfully achieved microexpansion in subgrade foundations, while the concurrent addition of $CaCl_2$ promoted greater early-age strength development. Related studies have also reported on the application of geopolymers in repairing structurally fractured concrete members (i.e., where the damaged sections lack continuous substrate connection). Alyousef et al. [28] confirmed the high compatibility of a waste ceramic tile-fly

ash-slag-based geopolymer with concrete substrates. Drawing a parallel conclusion, Zheng et al. [29] demonstrated that the interfacial modulus of rupture between GFRP-reinforced slag-based geopolymer and concrete was significantly greater than that of the conventional cement-concrete interface. Wang et al. [30] reported that, under structural repair conditions, the bond strength of the geopolymer-repaired specimens exceeded that of the cement-repaired specimens by up to 97.02% at elevated temperatures, demonstrating exceptional thermal resistance.

In summary, although the impact of various expansive agents on the drying shrinkage of geopolymers has been extensively investigated, the corresponding fresh properties of the modified pastes remain underexplored. Furthermore, comparative studies evaluating the effects of different expansive agents on the workability of an identical geopolymer matrix are notably scarce. Moreover, the current literature on geopolymer-based repair predominantly focuses on unmodified base pastes, with limited efforts devoted to using expansive agent-modified grouts for crack remediation. Crucially, while existing research primarily centers on evaluating concrete performance after repairing severe structural fractures, investigations concerning the remediation of fine cracks remain highly limited. The narrow apertures of these early-stage cracks impose far more stringent requirements on the workability and penetrability of the repair grouts. Intervening and reinforcing concrete elements at this nascent stage of cracking is of paramount importance for both structural safety and economic viability. Therefore, this study employs a slag-fly ash-based geopolymer as the unmodified base paste. A systematic comparative analysis was conducted to elucidate the evolution of both the fresh properties (fluidity, setting time, and drying shrinkage) and the mechanical performance of geopolymer pastes modified with three distinct expansive agents: MgO, CaO, and CSA. Subsequently, the optimal expansive agent-modified geopolymer grout was selected to repair concrete specimens featuring performed microcracks. To comprehensively evaluate its holistic repair efficacy, the mechanical recovery and durability performance of the repaired specimens were systematically benchmarked against those of specimens repaired with conventional ordinary Portland cement and epoxy resin.

2. Materials and Methods

2.1. Raw Materials

2.1.1. Precursors and Alkali Activator

The precursors employed for the geopolymer synthesis consist of slag and fly ash. Their macroscopic appearances and microscopic morphologies, illustrated in Figure 1, reveal that the slag constitutes irregular, angular particles, whereas the fly ash features a regular spherical morphology. The chemical compositions of both precursors were determined via X-ray fluorescence (XRF) spectroscopy and are summarized in Table 1, identifying CaO and SiO_2 as the predominant oxides in the slag and fly ash, respectively. Furthermore, the alkaline activator was formulated by blending a commercially available sodium silicate solution (with an initial silica modulus of 3.3) with sodium hydroxide flakes of 98% purity.

Table 1. Main composite of slag and fly ash.

Raw Materials	Mass Fraction/%					
	Al_2O_3	SiO_2	CaO	MgO	Fe_2O_3	SO_3
Slag	13.58	29.11	42.43	8.44	0.98	3.46
Fly ash	32.36	53.61	3.36	0.70	4.33	0.58

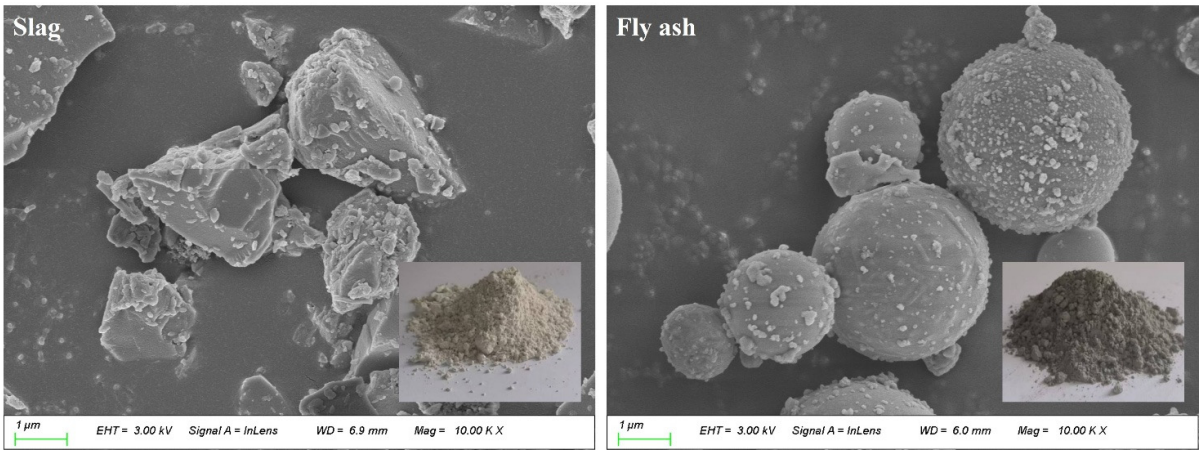


Figure 1. Geopolymer precursors.

2.1.2. Expansive Agent

Depending on the origin of expansion, expansive agents are generally classified into four primary categories: MgO-based, CaO-based, CSA-based, and composite types [31,32]. To rigorously isolate variables and elucidate the distinct effects and underlying mechanisms of disparate expansion sources on geopolymer performance, three single-component agents (MgO, CaO, and CSA) were selected as the expansive modifiers for the geopolymer in this study. As depicted in Figure 2, both CaO and MgO appear as white powders, whereas the CSA presents as a yellowish-brown powder. All three utilized expansive agents are of analytical grade. The MgO and CaO expansive agents used in this study were supplied by Tianjin Huasheng Chemical Reagent Co., Ltd., Tianjin, China, while the CSA expansive agent was supplied by Shanxi Feike New Material Technology Co., Ltd., Yuncheng, China.



Figure 2. Macroscopic characteristics of the expansive agents.

2.1.3. Materials for Concrete Preparation

42.5R OPC, supplied by Hunan Conch Cement Co., Ltd., (Loudi, China) was utilized for both casting the pre-cracked concrete substrates and formulating the subsequent repair grouts. The XRF results show that the main constituents of OPC are CaO and SiO_2, as present in Table 2. For the concrete matrix, continuously graded crushed stone with particle sizes ranging from 5 to 18 mm was employed as the coarse aggregate, while manufactured sand with a fineness modulus of 2.8 served as the fine aggregate.

Table 2. Main composite of 42.5R OPC.

Raw Materials	Mass Fraction/%					
	Al_2O_3	SiO_2	CaO	MgO	Fe_2O_3	Others
42.5R OPC	11.52	27.50	49.20	1.18	3.38	7.22

2.1.4. Solution Medium for Durability Test

A 5 wt.% Na_2SO_4 solution was utilized for both the sulfate wetting–drying cycles and the sulfate immersion tests, whereas a 5 wt.% NaCl solution was employed for the chloride immersion tests. Both Na_2SO_4 and NaCl were supplied by Tianjin Zhonglian Chemical Reagent Co., Ltd. (Tianjin, China), and the solutions were formulated using analytical-grade powders.

2.2. Synthesis Procedures

2.2.1. Expansion Agent Modified Geopolymer

This study aims to modify the slag-fly ash-based geopolymer by incorporating three distinct expansive agents (MgO, CaO, and CSA) to formulate grouts for the subsequent repair of cracked concrete specimens. Drawing upon existing literature and preliminary experimental trials, and accounting for the stringent workability and mechanical criteria demanded by crack repair applications, the baseline mix proportions were firmly established. Specifically, the mass ratio of fly ash to slag was fixed at 7/3, and the water-to-binder (W/B) ratio was maintained at 0.5. The alkaline activator was applied at a constant dosage of 40% (by mass of the precursor) with a designated modulus of 1.2 [33]. The dosages of expansive agents were determined from literature-reported effective ranges for alkali-activated materials and refined through preliminary tests to mitigate workability and strength losses. MgO was evaluated at 6–12% to encompass the typical effective window in alkali-activated slag and fly ash–slag systems. CaO was confined to 0.5–2% due to its high reactivity and the stricter fluidity/stability requirements of injectable paste. CSA was examined at 2–8% to span common sulfoaluminate-based additive dosages. The detailed experiment is summarized in Table 3.

Table 3. Detailed experiment on geopolymer modification.

No.	Expansive Agent		Curing Age (d)
	Type	Dosage (%)	
G (Blank)	/	/	7/28
MG series	MgO	6/8/10/12	7/28
CG series	CaO	0.5/1/1.5/2	7/28
SG series	CSA	2/4/6/8	7/28

Note: For all mixtures, the mass ratio of fly ash to slag is fixed at 7/3. The W/B is 0.5. The alkaline activator dosage is 40% (by mass of precursor) with a fixed modulus of 1.2.

The preparation procedure for the geopolymer pastes was as follows. Initially, slag and fly ash powders were weighed out in a predetermined mass ratio and placed in an NJ-160B cement paste mixer (Wuxi Jianyi Instrument Machinery Co., Ltd., Wuxi, China). After mixing for 15 s, supplementary water and the alkaline activator solution, which had been prepared and allowed to cool to ambient temperature 24 h prior to use, were added to the dry mixture. This was followed by a low-speed mixing phase of 120 s. During a subsequent 15 s pause, the designated expansive agent was incorporated into the mixture; for the control group, the paste was simply left to rest. A final high-speed mixing phase of 120 s was then executed to ensure the complete homogenization of the paste. Upon completion

of mixing, the fresh paste was cast into 40 mm × 40 mm × 40 mm cubic molds and properly compacted to eliminate entrapped air voids. After casting, the specimens were kept in the laboratory at approximately 25 °C under ambient indoor humidity conditions until sufficient shape stability was reached for demolding. The pre-demolding duration varied with the mixture and was approximately consistent with its initial setting behavior. The demolded specimens were then transferred to a constant-temperature curing chamber for subsequent curing. They were maintained under controlled conditions (20 ± 2 °C and relative humidity > 95%) until reaching their designated testing ages. No obvious efflorescence was observed on the specimen surfaces during the 28-day curing period under the curing conditions employed in this study.

2.2.2. Concrete Crack Repair Experiment

Based on workability and mechanical performance, the optimal expansive agent-modified geopolymer grout was selected to conduct crack repair experiments on C30 concrete substrates. The concrete substrates were cast as cylinders with a radius of 50 mm and a height of 200 mm. Artificial cracks with varying apertures (2.0, 2.5, and 3.0 mm), a uniform width of 50 mm, and a penetration depth of 100 mm were pre-induced by inserting steel shims during casting. The detailed specimen preparation protocol is illustrated in Figure 3. The concrete specimens were fabricated following standard procedures. After an initial curing period of 24 h, the cylinders were demolded and transferred to a standard curing chamber for 28 days prior to the crack repair operations. Before repairing, the preformed cracks of the concrete specimens were pre-wetted. Then, the repair grout was injected into the cracks using a syringe until slight overflow was observed at the crack opening, which was taken as the criterion for complete filling. After grouting, the specimen surface was leveled, and the repaired specimens were subsequently cured under standard curing conditions for later testing. For comparative analysis, 42.5R OPC and epoxy resin were employed as control repair materials. Notably, the 7-day and 28-day compressive and splitting tensile strengths reported in this study exclusively denotes the curing durations elapsed after the completion of the crack repair process.



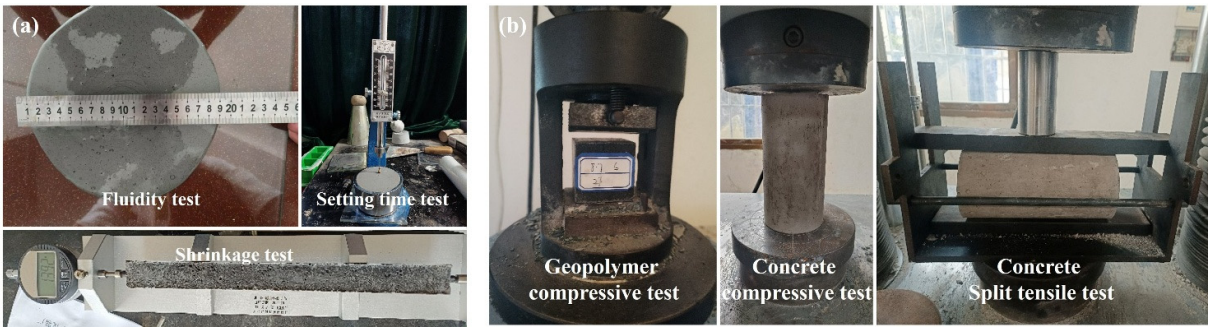
Figure 3. Crack setting on concrete specimen.

2.3. Testing Methods

2.3.1. Workability

The workability evaluation of the fresh pastes encompassed three key parameters: fluidity, setting time, and drying shrinkage. Figure 4a shows the operation method. The fluidity was determined in accordance with the protocols outlined in Chinese National Standard GB/T 8077-2023 [34]. Specifically, the freshly mixed paste was cast into a standard truncated cone mold. Upon leveling the top surface, the mold was lifted vertically, allowing the paste to flow freely for 30 s. The maximum spread diameters along two mutually perpendicular directions were measured, and their arithmetic mean was recorded as the

final fluidity value. The initial and final setting times as a comparative fresh-state index of the geopolymer pastes were measured utilizing a standard Vicat apparatus, strictly conforming to the procedures specified in GB/T 1346-2024 [35]; they were used solely as a comparative fresh-state index. Furthermore, the drying shrinkage tests were conducted following the methodologies stipulated in the Chinese Standard JC/T 313-2009 [36]. The length variations of the specimens, which possessed an effective gauge length of 250 mm, were monitored at designated curing ages using a length comparator equipped with a precision dial indicator. Unless otherwise specified, each test group consisted of three parallel specimens.



(**a**) Slurry fresh properties and shrinkage tests (**b**) Mechanical tests

Figure 4. Representative fresh slurry properties tests and concrete mechanical tests.

2.3.2. Mechanical Tests

Compressive strength tests on the geopolymer cube specimens cured for 7 and 28 days were executed in accordance with Chinese Standard GB/T 17671-2021 [37]. A TYA300-B universal testing machine (Wuxi New LUDA Instrument Equipment Co., Ltd., Wuxi, China) was employed to apply the axial load at a constant rate of 50 N/s. Meanwhile, the compressive strength and split tensile strength evaluation of the cylindrical concrete specimens followed the protocols stipulated in GB/T 50081-2019 [38], utilizing a WAW-1000D universal testing machine (Shanghai Sansi Zongheng Mechanical Manufacturing Co., Ltd., Shanghai, China) with a designated loading rate of 0.5 MPa/s. Figure 4b illustrates the experimental setup and on-site execution. Each test group comprised three replicate specimens to ensure statistical robustness and experimental reproducibility.

2.3.3. Durability Tests

To assess the performance of the repaired concrete specimens under complex service environments, four durability testing regimens were executed: sulfate wetting–drying cycles, freeze–thaw cycles, continuous sulfate immersion, and chloride immersion. All procedures strictly complied with the Chinese National Standard GB/T 50082-2024 [39]. A single cycle comprised immersion in a 5 wt.% Na_2SO_4 solution for 15 ± 0.5 h, air-drying for 1 h, oven-drying at 80 ± 5 °C for 6 h, and subsequent cooling for 2 h. In total, the specimens were subjected to 75 such cycles. The freeze–thaw testing adopted the slow-freezing method utilizing a JCD-40 (Hebei Tijian Engineering Instrument Co., Ltd., Tianjin, China). Each cycle consisted of freezing at −20 °C for 4 h followed by thawing at 20 °C for 4 h, repeated for a total of 50 cycles. For the salt immersion tests, specimens were completely submerged in artificially formulated 5 wt.% Na_2SO_4 and NaCl aggressive solutions, respectively. The concrete specimens were fully immersed in the solution, with the liquid level maintained at least 50 mm above the top surface of each specimen throughout the 28-day soaking period. To ensure concentration stability, the exposure solutions were replenished with fresh batches every 7 days. All four durability tests described above were performed on repaired concrete specimens after 28 days of standard curing and three parallel specimens

were set for each group. Strength retention, defined as the ratio of compressive strength after durability testing to that before testing, served as the primary durability indicator in this study, directly reflecting the residual load-bearing performance of the repaired concrete, whereas mass loss and elastic-modulus degradation were deferred to future work.

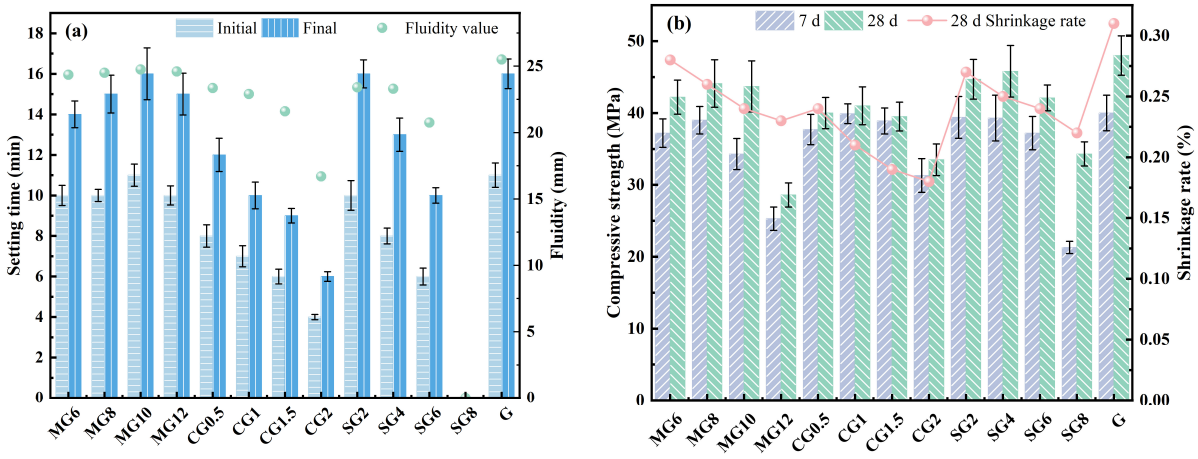
2.3.4. Microstructural Characterization

In an attempt to more clearly define the mineralogical phase assemblage, microstructural characteristics, and micromorphology of the paste, SEM and XRD tests were performed on the expansive agent-modified geopolymer [40–42]. Also, XRD, SEM and MIP tests were carried out on the repaired concrete specimens. The XRD measurements were performed using an X'Pert PRO MPD diffractometer (PANalytical B.V., Almelo, The Netherlands), with the scanning executed over a 2θ range of 5° to 90° at a rate of 5°/min and a step size of 0.02°. For SEM observation, the specimens were taken from the central block fragments of the concrete specimens after the compressive strength test. After selection, the samples were sealed and immersed in anhydrous ethanol to terminate further reaction, followed by low-temperature drying. Prior to imaging, the sample surfaces were sputter-coated with gold to improve electrical conductivity and ensure clear imaging. The SEM analysis was conducted using a ZEISS Gemini 300 scanning electron microscope (Carl Zeiss AG, Berlin, Germany). The pore structure was evaluated employing an AutoPore V 9600 mercury porosimeter (Micromeritics Instrument Corporation, Norcross, GA, USA). The detectable pore size range was set from 0.005 μm to 1100 μm, with the mercury intrusion pressure progressively increasing from 0.2 psi to 33,000 psi. The surface tension (γ) and contact angle (θ) of mercury were specified as 0.485 N/m and 140°, respectively. All specimens subjected to the microstructural characterizations were sourced from the intact fragments collected after the mechanical tests. For the XRD analysis, the fragments were pulverized and sieved into powders with particle sizes below 0.075 mm. The particle size of the SEM and MIP test specimens was approximately 10.0 mm.

3. Results

3.1. Fresh Properties and Compressive Strength of Expansive Modified-Geopolymer

Figure 5 systematically evaluates the effects of three expansive agents on the workability and compressive strength of the fly ash-slag based-geopolymer. As depicted in Figure 5a, compared to the control group (G), incorporation of expansive agents inevitably consumes free water within the system, leading to varying degrees of fluidity reduction in the fresh pastes [43]. Notably, the MgO-modified geopolymer (MG) exhibits minimal fluidity fluctuation across the high-dosage range of 6–12%, with a reduction in less than 4%, while maintaining initial and final setting times comparable to those of the control. In contrast, both the CaO-modified geopolymer (CG) and CSA-modified geopolymer (SG) severely compromise paste fluidity while drastically accelerating the setting process. Specifically, the initial and final setting times for CG2 plunge to merely 4 min and 6 min, respectively, whereas the SG8 paste undergoes flash setting, fundamentally losing its plasticity. This phenomenon arises because the flash-setting tendency of the CaO- and CSA-modified pastes is governed by the combined effects of rapid early hydration, pore-solution chemistry, and particle morphology, rather than by reaction rate alone [44–46].



(**a**) Setting time and fluidity (**b**) Shrinkage and compressive strength

Figure 5. Fresh properties and compressive strength of geopolymer with three types of expansive agents at different dosages.

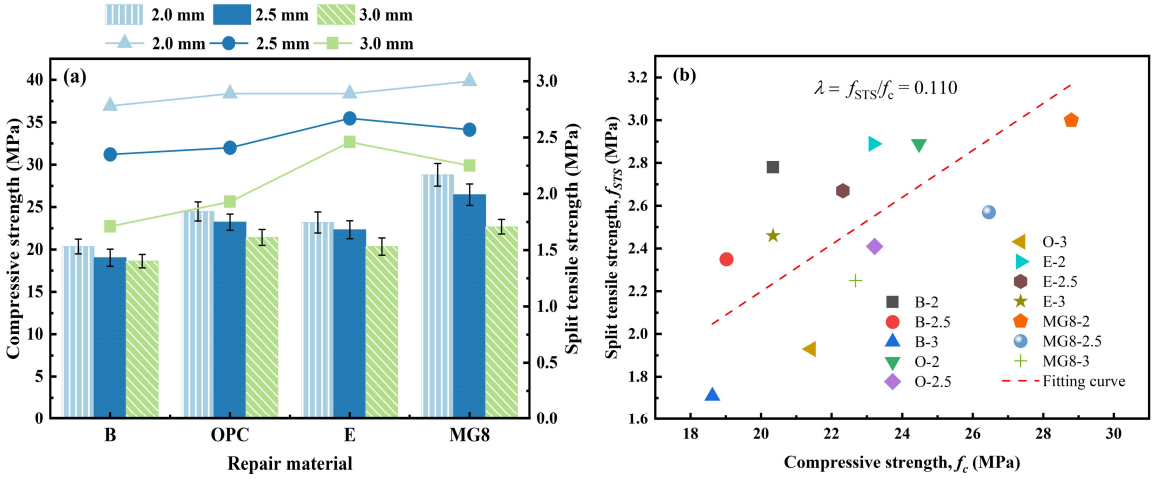
Mitigating shrinkage deformation remains the primary objective of introducing expansive agents. As illustrated by the 28-day drying shrinkage rates in Figure 5b, all three additives effectively suppress the shrinkage of the geopolymer matrices, with higher dosages yielding progressively lower shrinkage values. Concurrently, however, this enhanced volume stability is accompanied by dynamic fluctuations in compressive strength. For the MG, CG, and SG groups, both the 7-day and 28-day compressive strengths exhibit a parabolic trajectory—initially increasing before subsequently declining—as the expansive agent dosage increases. The peak strengths within each respective series are achieved by MG8 (44.10 MPa), CG1 (41.00 MPa), and SG4 (45.80 MPa). Crucially, the incorporation of CaO severely hinders late-age strength development in the paste, yielding a maximum 7-day to 28-day strength gain of only 7.03%, as observed in CG2. The relatively small increase in compressive strength from 7 d to 28 d indicates that the major geopolymerization reaction had already occurred at early age under the selected conditions, while the later-age strength gain mainly resulted from continued microstructural densification rather than a distinct secondary reaction stage. Conversely, the MgO and CSA modifications preserve more robust potential for late-stage strength gain; the strength increments for MG8 and SG4 reach 13.08% and 16.54%, respectively, demonstrating a superior strength-shrinkage balancing mechanism. It should be noted that engineering-scale injection may involve additional factors, such as crack geometry, injection pressure, and structural restraint, which require further investigation in future work.

3.2. Mechanical Properties of Concrete Repaired with Different Width Cracks

Derived from the aforementioned evaluations of workability and mechanical properties, incorporation of MgO induces a marginal fluidity reduction of merely 3.73% in the geopolymer pastes compared to CaO and CSA modifications. Furthermore, fluidity exhibits remarkable stability across varying MgO dosages, with the maximum absolute intra-group variation being a negligible 1.64%. Notably, high dosage of MgO does not precipitate adverse phenomena such as critically short setting time intervals or flash setting, thereby ensuring excellent operational predictability and temporal control during the practical repair process. Additionally, the drying shrinkage compensation capacity of MgO is virtually on par with that of CSA and only slightly inferior to that of CaO. Compressive tests demonstrate that the MG8 achieves a robust 28-day compressive strength of 44.1 MPa, accompanied by a 7 to 28-day strength development rate of 13.08%, which substantially outperforms the CaO-modified counterparts. Although SG4 showed a slightly

higher compressive strength than MG8, it was inferior to MG8 in all other key performance aspects. Based on the comprehensive analysis above, MG8 provides a considerably broader operational window for fluidity and setting time, while simultaneously preserving high mechanical capacity and a highly favorable strength development trajectory. Consequently, the MG8 was selected as the optimal formulation for subsequent investigations into its efficacy in remediating concrete cracks.

Figure 6 illustrates the mechanical properties of the cracked concrete substrates repaired with OPC, epoxy resin (E), and MG8, alongside the unrepaired group (B). As depicted in Figure 6a, widening the initial crack from 2 mm to 3 mm universally compromises the load-bearing capacity across all specimens. Under the 3 mm crack scenario, the compressive and splitting tensile strengths of the unrepaired matrix plummet to a mere 18.62 MPa and 1.71 MPa, respectively. In contrast, the repaired counterparts exhibit evident strength recoveries. Notably, the compressive strength of the MG8-2 specimen peaks at 28.80 MPa, demonstrating a significant superiority over both the cement- and epoxy-repaired groups. Even under the severe 3 mm crack condition, the MG8-3 specimen retains the maximum compressive strength of 22.68 MPa among all groups. Conversely, the epoxy resin-repaired specimens demonstrate exceptional tensile resilience during the splitting tensile tests. Specifically, the splitting tensile strength of E-3 registers at 2.46 MPa, outperforming both MG8-3 (2.25 MPa) and OPC-3 (1.93 MPa). This tensile advantage arises not only from the high elongation at break of the epoxy resin, but also from its strong crack-face adhesion and energy-dissipation capacity, which are more effectively mobilized under splitting-induced interfacial opening than under compressive loading [47]. This observation is further corroborated by the scatter distribution of the tension-compression ratio in Figure 6b. The data points for the epoxy-repaired group predominantly shift toward the upper-left region above the fitting curve, statistically verifying that the flexible organic polymer contributes to supplemental tensile toughening. Ultimately, the overall fitted tension-compression ratio λ stabilizes at 0.110, reflecting that the repaired concrete matrix inherently retains its macroscopic brittle nature.



(**a**) Compressive and split tensile strength (**b**) Fitting relationship

Figure 6. Compressive strength and split tensile strength of specimen (B: Blank control; E: Epoxy resin repaired).

3.3. Durability

3.3.1. Dry–Wet Cycle Test

Assessing the long-term reliability of various repair systems under harsh service conditions, Figure 7 plots the compressive strength evolution alongside the macroscopic

deterioration morphology of cracked concrete cylinders subjected to 75 sulfate Dry–Wet cycles. While the synergistic effect of sulfate attack and cyclic wetting-drying inevitably compromises the mechanical integrity of all specimens, the extent of degradation varies drastically across the different binders. As depicted in Figure 7a, the strength retention rates for the conventional material repaired specimens generally stagnate between 73% and 79%, with their absolute residual strengths falling below the 20 MPa threshold. By stark contrast, MG8-repaired group exhibits exceptional resilience against the aggressive attack. Its strength retention consistently surpasses the 80% mark regardless of the initial crack width. Consequently, even for concrete substrates containing cracks 2.5 mm or 3.0 mm in width, the residual compressive strength following 75 dry–wet cycles remains consistently higher than that of conventional repair materials, ranging from 20 to 25 MPa.

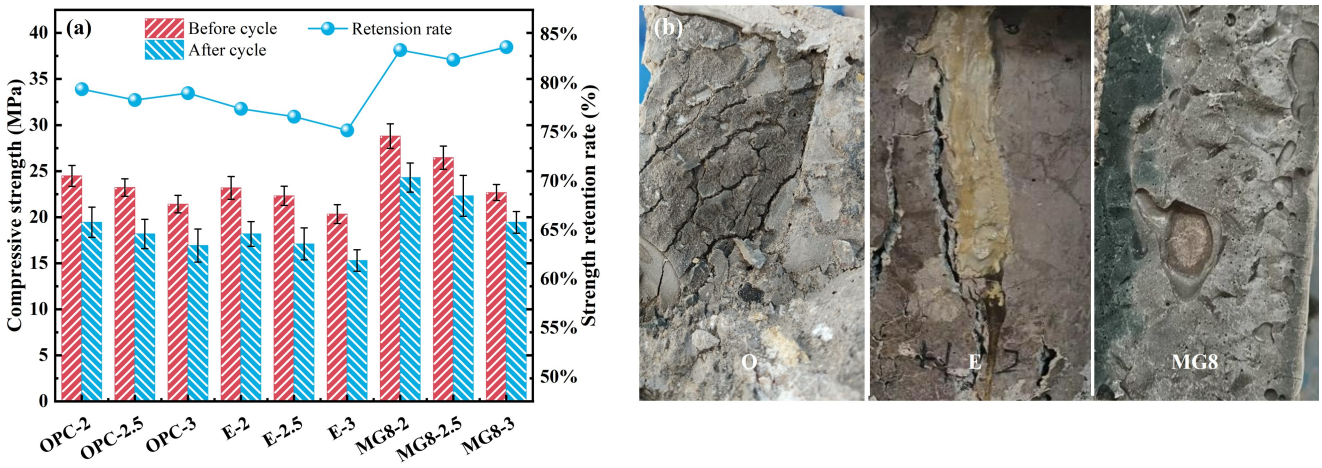


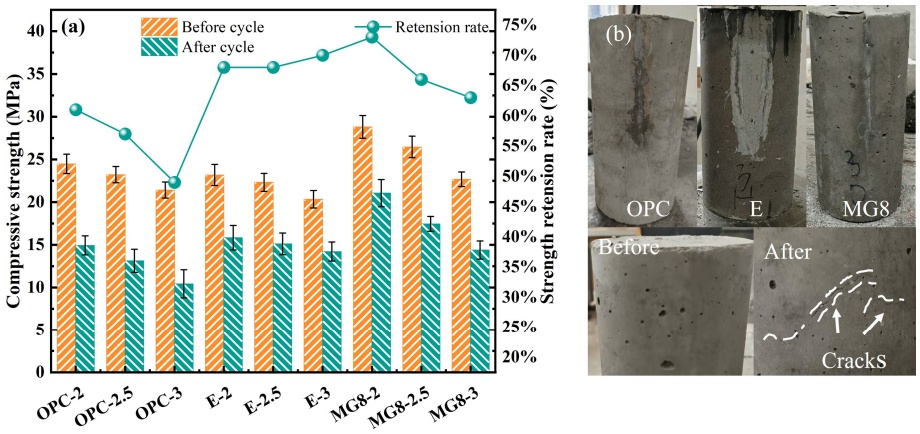
Figure 7. Compressive strength and macroscopic morphology of concrete following 75 dry–wet cycles.

This pronounced disparity in macroscopic mechanical performance is directly mirrored in the post-degradation visual appearance of the specimens, as shown in Figure 7b. These photos are provided solely for qualitative comparison, as they were acquired at different magnifications. Driven by the dual aggression of severe sulfate crystallization and chemical attack, the surface of the OPC-repaired matrix suffers from extensive reticular cracking and spalling. This typical failure mode is primarily governed by the destructive expansion stresses generated by internally formed corrosion products, such as ettringite and gypsum [48]. For organic materials like epoxy resin, despite their inherent chemical resistance, fundamental incompatibilities with the inorganic concrete substrate in terms of elastic modulus and thermal expansion coefficient render them highly susceptible to interfacial debonding. Under the fatigue of repeated wetting–drying stresses, premature failure preferentially propagates along this vulnerable repair interface [49]. Conversely, the MG8-repaired group preserves a highly intact macroscopic morphology, featuring a dense, almost indistinguishable boundary between the repair zone and the parent concrete. This robust integrity indicates that the highly cross-linked aluminosilicate gel network within the geopolymer not only intrinsically resists sulfate ion penetration but also establishes superior interfacial chemical bonding with the host substrate [50]. Such bonding effectively seals the potential percolation pathways along the crack interface, thereby maximizing the safeguard of the overall load-bearing skeleton.

3.3.2. Freeze–Thaw Cycle Test

The mechanical properties and macroscopic morphology of the specimens following 50 freeze–thaw cycles are presented in Figure 8. As shown in Figure 8a, when the crack width increases from 2 mm to 3 mm, the initial compressive strength of the OPC group

experiences a minor drop from approximately 24.48 MPa to 21.42 MPa. However, following freeze–thaw exposure, its residual strength plummets from 14.94 MPa to below 10.44 MPa. This precipitous mechanical decay is directly captured by the strength retention curve, which drops sharply from 61% to around 49%. Such behavior clearly exposes the vulnerability of conventional cementitious materials under wider crack conditions, where they act as reservoirs for free water and become highly susceptible to frost-heaving stresses [51].



(**a**) Mechanical characteristics (**b**) Macroscopic morphology

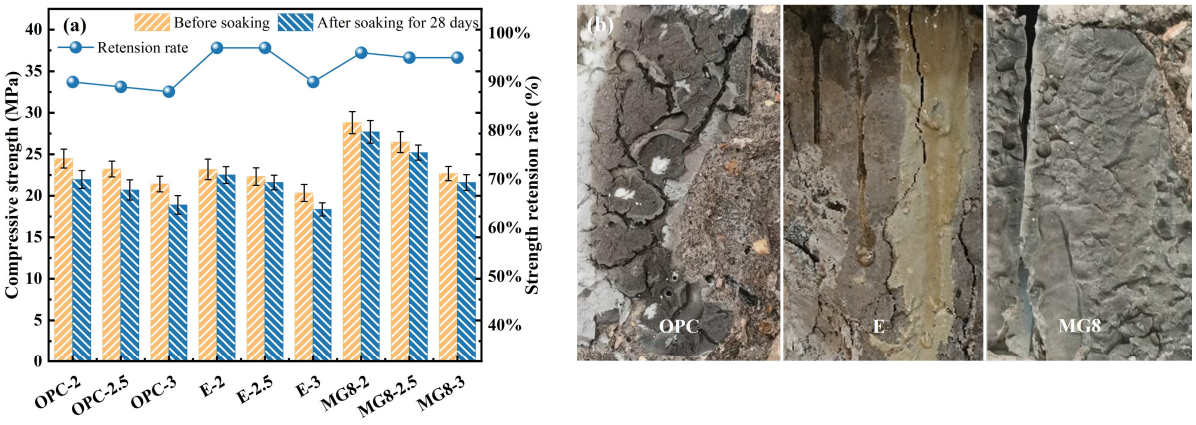
Figure 8. Compressive strength and macroscopic morphology of concrete following 50 freeze–thaw cycles.

Counterintuitively, the freeze–thaw resistance of the E-repaired group enhances as the initial crack widens, evidenced by a rise in the strength retention rate from 68% to 73%. This implies that a larger volume of epoxy resin incorporated into the concrete matrix actually benefits the post-cycling residual strength after 50 freeze–thaw cycles. Although this absolute strength remains marginally inferior to that of the cement-repaired counterparts, the trend underscores a critical mechanism: as crack width increases and water ingress becomes more severe, the hydrophobic and sealing properties of epoxy more effectively suppress capillary transport and water accumulation within the crack zone, thereby reducing freeze–thaw-induced volumetric damage [52,53]. The MG8-repaired group demonstrates dominant mechanical superiority under the 2 mm condition, boasting initial and residual strengths of roughly 28.60 MPa and 22.68 MPa, respectively, alongside a peak retention rate touching 73%. Even under the extreme 3 mm crack scenario, while the absolute residual strength of MG8-3 drops to roughly 14.40 MPa due to intensified physical ice expansion, it still significantly outperforms the cement-repaired counterpart of the same width. Figure 8b shows that, regardless of the repair method used for the concrete substrate, cracks appear on its surface after 50 freeze–thaw cycles.

3.3.3. Na_2SO_4 Solution Immersion Test

Distinct from the previously discussed 75-cycle sulfate dry–wet exposure, the 28-day continuous immersion in sodium sulfate solution is designed to isolate thermodynamic fatigue, exclusively evaluating the resistance of the respective repair systems to singular chemical attack. The data in Figure 9a show that, under continuous Na_2SO_4 immersion, the strength loss of all repaired specimens is much less severe than that under sulfate dry–wet cycling, and therefore the strength retention rates remain generally high. Specifically, the residual strength of the OPC-repaired group ranges from 18.90 to 21.96 MPa, with its strength retention showing an improvement compared to the dry–wet condition. Owing to the inherent chemical stability of organic polymers, the E-repaired group exhibits minimal sensitivity to singular sulfate ion attacks, yielding retention rates that stabilize between 90%

and 97%. However, in terms of absolute load-bearing capacity, the MG8-repaired group maintains a clear advantage. Under the 2 mm crack condition, the residual strength of the specimen reaches approximately 27.70 MPa, and it remains above 21.00 MPa even for the 3 mm wide cracks. With a retention rate exceeding 95% across the group, it demonstrates reliable chemical stability alongside robust mechanical performance.



(**a**) Mechanical characteristics (**b**) Macroscopic morphology

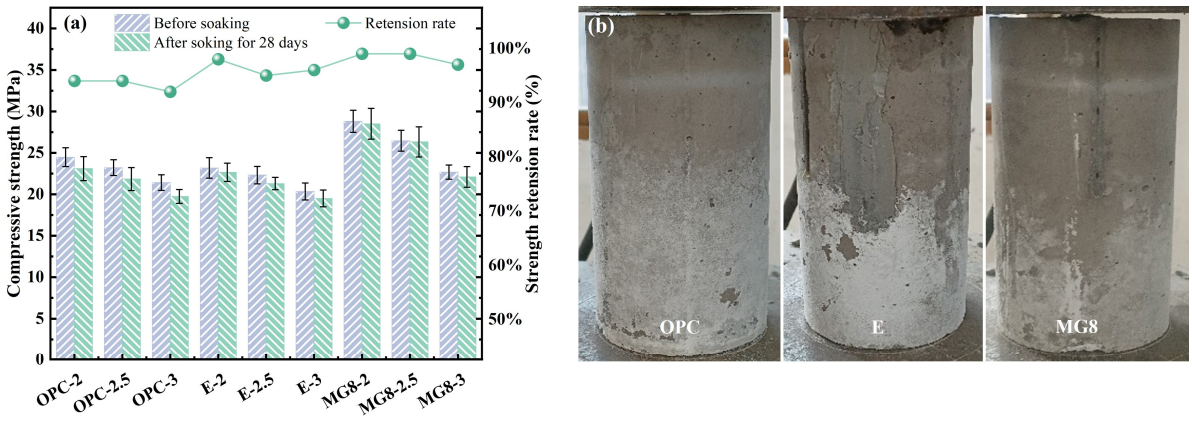
Figure 9. Compressive strength and macroscopic morphology of concrete after soaking in Na_2SO_4 solution for 28 days.

The cross-sectional morphology of the specimens following immersion are presented in Figure 9b. When thermodynamic effects are excluded, the surface of specimens in the cement repair group exhibit a pronounced reticular cracking morphology. This indicates that under Na_2SO_4 single-phase immersion, the internal stresses generated by the volume expansion of ettringite and gypsum, which formed through the reaction of infiltrated sulfate ions with hydration products, alone suffice to induce matrix deterioration [54]. In contrast, the resin repair group exhibited better surface integrity with no visible signs of corrosive attack, a failure pattern markedly different from its susceptibility to interfacial debonding and peeling under dry–wet cycles. The geopolymer repair group likewise remained macroscopically dense and intact, free from chemical expansion-induced cracks. This further confirms that the dense aluminosilicate network of the geopolymer provides a strong physical barrier against sulfate ions, thereby effectively preserving the structural integrity of the repair system under sulphate erosion conditions [55].

3.3.4. NaCl Solution Immersion Test

The degradation mechanism induced by a chloride environment differs fundamentally from that of sulfate attack. It primarily manifests as the capillary penetration of chloride ions and subsequent physical crystallization, rarely triggering severe chemical expansion damage in the short term. As depicted in Figure 10a, following 28 days of NaCl immersion, none of the repaired specimens experience drastic mechanical degradation, with overall strength retention rates universally exceeding the 90% threshold. Specifically, the strength retention of the OPC-repaired group ranges between 92% and 94%, indicating that short-term chloride exposure exerts limited direct chemical erosion on the load-bearing skeleton of the cementitious matrix. Relying on the intrinsic chemical inertness of organic polymers, group E sustains a high retention bracket of 95% to 97%. MG8-repaired group demonstrates the superior resistance to chloride penetration. Under the 2 mm crack condition, the concrete substrate repaired by geopolymer not only achieves the highest absolute residual strength of 28.50 MPa but also approaches a 99% retention rate. Even under the more severe

3 mm wide-crack scenario, its retention remains stable above 97%, translating to a nearly lossless preservation of mechanical properties.



(**a**) Mechanical characteristics (**b**) Macroscopic morphology

Figure 10. Compressive strength and macroscopic morphology of concrete after soaking in NaCl solution for 28 days.

These mechanical response characteristics are further elucidated by the macroscopic morphologies presented in Figure 10b. After 28 days of immersion, obvious white salt crystallization appears on the surfaces of all specimens, resulting from the surface enrichment of NaCl crystals driven by capillary suction. In stark contrast to the reticular cracking induced by sulfate attack, although the surfaces of cement repair group and epoxy repair group exhibit salt frosting and slight superficial sanding, their overall macroscopic structures remain intact without penetrating cracks. This structural integrity directly accounts for their universally high strength retention. By comparison, the degree of surface crystallization in the geopolymer repair group is relatively mild. The geopolymer can effectively retard the inward transport of chloride ions and free water, thereby reliably safeguarding the overall mechanical performance of the repaired components under chloride exposure.

It should be emphasized that the present NaCl immersion results reflect only the short-term chloride resistance of unreinforced repaired concrete under the selected standardized exposure, and do not constitute a full assessment of long-term chloride durability in reinforced structures, where chloride-induced steel corrosion is typically the governing concern.

4. Microscopic Characterization

4.1. XRD Analysis

4.1.1. Geopolymer Modified with Expansive Agent

Figure 11 presents the XRD patterns of geopolymer slurries modified with varying dosage of MgO, CaO, and CSA. In Group G, XRD patterns reveal distinct crystalline peaks corresponding to quartz and mullite, alongside broad, low-intensity humps characteristic of the amorphous geopolymer gels (e.g., N-A-S-H, C-A-S-H) [56,57]. Quartz, acting as an inert phase, does not participate in polycondensation but functions solely as a pore-filling aggregate. Amorphous gels encapsulate and cement the loose, unreacted precursor particles, mainly residual fly ash and slag particles, thereby contributing to a denser and more integrated matrix structure.

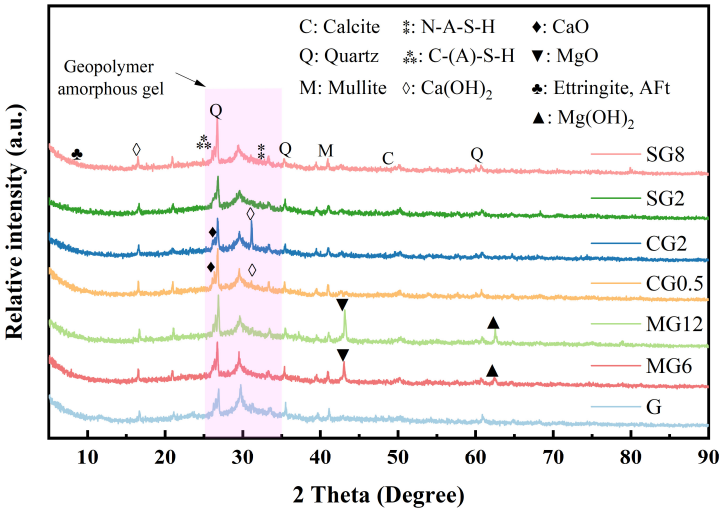


Figure 11. XRD patterns of expansive agent modified geopolymer.

Upon the incorporation of MgO, a crystalline peak ascribed to $Mg(OH)_2$ emerges at approximately 49° 2θ. The diffraction intensity of this peak intensifies monotonically with increasing MgO dosage, indicating that the addition of MgO promotes the precipitation of micro-expansive $Mg(OH)_2$ [58]. At lower MgO dosages, the decrease in paste fluidity remains limited, which may be attributed to the combined effects of slight water consumption during early hydration and the relatively moderate early-age influence of MgO on fresh-state structure. Such a restrained impact on workability is beneficial for maintaining adequate paste flowability and creating favorable conditions for subsequent geopolymerization, thereby contributing to the improvement of macroscopic mechanical properties. However, when the MgO dosage reaches 12% (MG12), the intensity of the unreacted MgO crystalline peak surges, accompanied by a noticeable attenuation of the C-A-S-H diffuse hump. It is postulated that an abundance of unreacted MgO crystallizes and coats the surfaces of the precursor particles, thereby hindering progressive geopolymerization.

The introduction of CaO leads to a substantial enhancement in the crystalline peak of $Ca(OH)_2$. Nevertheless, owing to its inherently low intrinsic strength and poor chemical stability, its contribution to the overall strength improvement of the geopolymer is rather limited [59]. For the CSA-modified group, crystalline peaks corresponding to ettringite (AFt) are detected [60]. On one hand, the formation of expansive AFt effectively compensates for shrinkage induced by the dehydration of the geopolymer slurry. On the other hand, excessive AFt precipitation retards the ongoing geopolymerization process, as evidenced by a reduced intensity of the geopolymer gel's diffuse hump in the 25–35° 2θ range.

4.1.2. XRD of the Concrete Crack Repair Interface

Given the results of previous durability tests, the failure of the epoxy resin-repaired interface is mainly attributed to physical debonding, which originates from the thermophysical incompatibility between the organic polymer and the inorganic matrix. As an amorphous organic resin, its interfacial adhesion relies heavily on physical interlocking and intermolecular forces, without generating new crystalline mineral phases [61]. Consequently, to deeply investigate the chemical bonding and degradation mechanisms, XRD focuses exclusively on the reactive inorganic binder systems, specifically comparing the mineralogical evolution within the interfacial transition zones of the OPC-concrete (O-C) and MG8-modified geopolymer-concrete (MG8-C) specimens. The results are shown in Figure 12.

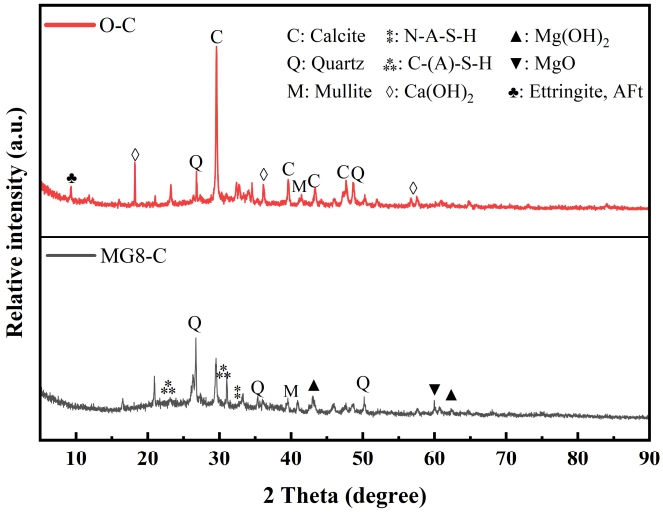


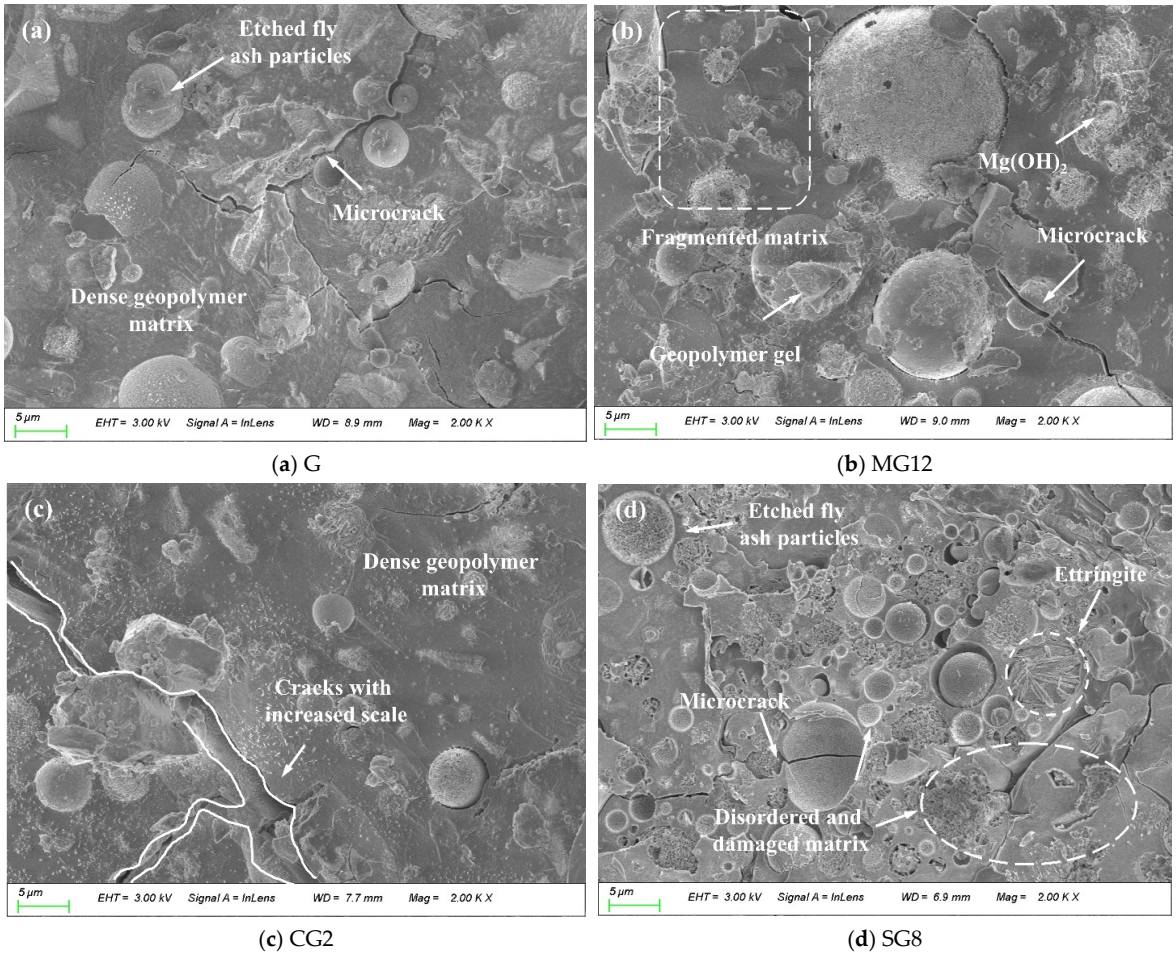
Figure 12. XRD patterns of O-C and MG8-C after 28 days of standard curing.

Scrutinizing the O-C interface pattern reveals that, apart from the ubiquitous quartz peaks introduced by the aggregates, its most prominent mineralogical feature is the presence of abundant $Ca(OH)_2$ and its carbonation product, calcite, exhibit sharp diffraction peaks. The enrichment of $Ca(OH)_2$ crystals at the interface not only weakens the load-bearing capacity of the interfacial zone, but also creates a calcium-rich environment that may promote the formation of additional expansive products (e.g., ettringite) during subsequent sulfate attack, while exacerbating freeze–thaw-induced leaching deterioration. It should also be noted that the ettringite detected in the normally cured specimens is a common hydration product in cementitious systems and should not be directly interpreted as evidence of sulfate attack. The most critical phase transition in the MG8-C interface pattern is the complete disappearance of the $Ca(OH)_2$ peaks. Instead, the phase assemblage is characterized by a distinct diffuse broad hump spanning the 25–35° 2θ range, interspersed with the characteristic diffraction signals of C-S-H and C-A-S-H gels.

4.2. SEM Analysis

4.2.1. Geopolymer Modified with Expansive Agents in Maximum Dosage

Figure 13 illustrates the microscopic morphology of the geopolymer pastes. As depicted in Figure 13a, the matrix without expansive agent (G) exhibits a generally smooth and dense fracture surface characterized by scant micropores and microcracks. Spherical fly ash particles are firmly embedded within the geopolymer gel, forming rounded, crack-free interlocking interfaces, which result in a compact micropore structure. A comparative analysis of Figure 13a,b reveals that the microscopic cross-section of MG12 is heavily populated with fly ash particles, whose surfaces are covered with varying amounts of crystalline products. Based on the morphology of these crystals and corresponding XRD results, they are indexed as $Mg(OH)_2$. The volumetric expansion accompanying the formation of these crystals effectively counteracts the shrinkage inherent to the dehydration and polycondensation processes within the paste [62]. However, an excessive dosage of MgO impedes the continuous geopolymerization reaction. Crystals covering the fly ash particles hinder further contact between the precursor and the alkaline activator, thereby disrupting the depolymerization process, as evidenced by the notably increased number of unreacted fly ash particles observed in the micrograph.



(**a**) G (**b**) MG12

(**c**) CG2 (**d**) SG8

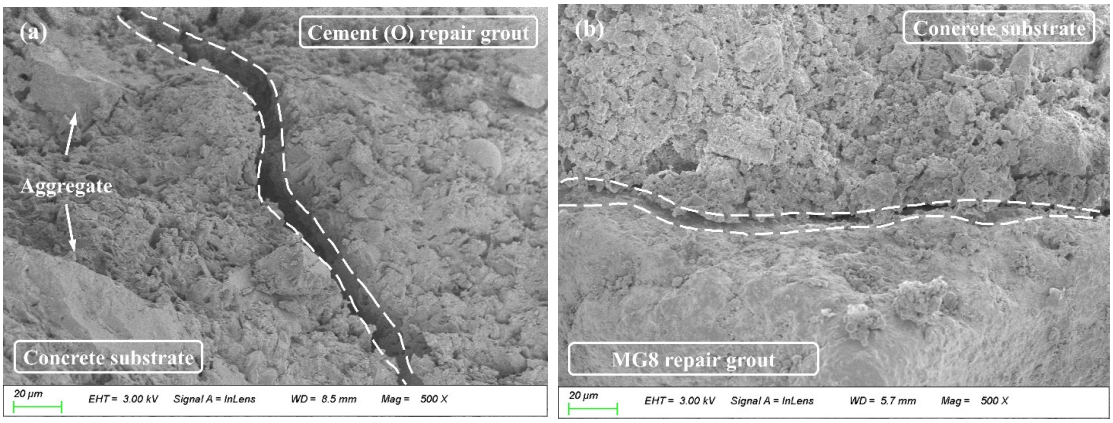
Figure 13. Micro-characteristics of geopolymer with maximum dosage of expansive agent.

Figure 13c presents the microstructure of CG2. While exhibiting comparable structural densification to G, the drastic reduction in setting time induces structural microcracks stemming from intense reaction kinetics, visible under microscopy. At low CaO dosage, the hydration-induced expansion stress partially offsets the shrinkage stress caused by dehydration, thereby compensating for the drying shrinkage of the matrix. Conversely, excessive CaO promotes crack propagation, compromising the critical load-bearing paths of the matrix, which culminates in a degradation of macroscopic mechanical performance [63]. Figure 13d illustrates that CSA induces the formation of needle-like ettringite (AFt) crystals. Saturated AFt crystals growing within confined environments generate outward crystallization pressure, mitigating paste shrinkage. However, SG8 exhibits increased porosity accompanied by inter-pore crack coalescence, leading to a higher degree of microstructural fragmentation on the observed surface. The excessive crystallization pressure generated by AFt ultimately compromises the overall integrity of the slurry microstructure. Therefore, the critical threshold in compressive strength corresponds to the transition from microstructural densification and defect compensation at low expansive-agent dosages to expansion-induced heterogeneity, local stress accumulation, and microcrack development at excessive dosages.

4.2.2. SEM of the Concrete Crack Repair Interface

Figure 14 presents a comparative SEM analysis of the repair interfaces in O-C and MG8-C. A close examination of Figure 14a reveals a pronounced and continuous physical debonding gap within the interfacial transition zone of the O-C, distinctly separating

the repair grout from the parent concrete. The cementitious matrix itself exhibits a relatively loose, porous microstructure accompanied by distinct angular crystalline features. Conversely, the MG8-C depicted in Figure 14b demonstrates a fundamentally different interfacial profile. Although the boundary of the preinduced crack remains faintly visible, the gap width is drastically diminished, exhibiting evident signs of cohesive reattachment. MG8 develops a highly dense and homogeneous N-A-S-H and C-A-S-H gels amorphous gel network [64]. This highly compacted gel system not only minimizes interfacial voids but also demonstrates a superior capacity to fill microfissures and physically anchor onto the parent substrate. Such microstructural evidence rigorously corroborates the superior interfacial integrity and enhanced crack-repair potential of the geopolymer system observed in the preceding mechanical evaluations.

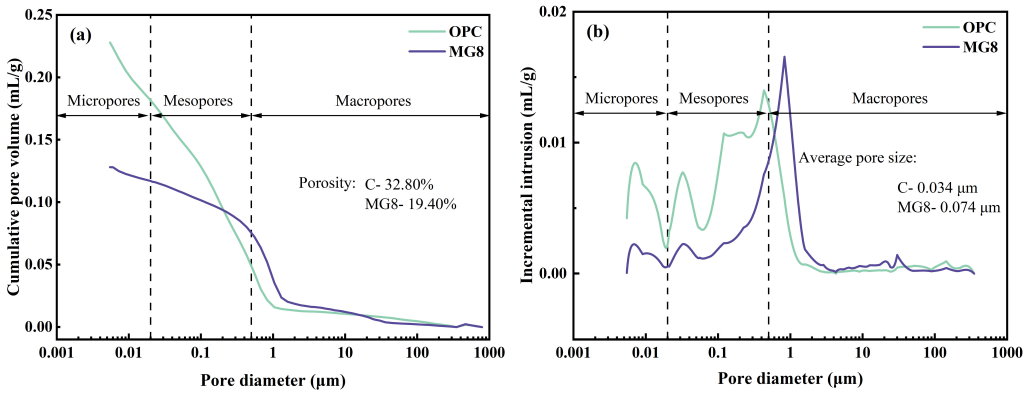


(**a**) O-C (**b**) MG8-C

Figure 14. Microscopic morphology of O-C and MG8-C.

4.3. MIP Analysis

The inherent pore structure of a hardened repair matrix critically governs its macroscopic impermeability and long-term service safety [65]. To gain deeper insights into this microstructural evolution and validate the engineering feasibility of the proposed binders, Figure 15 and Table 4 present the MIP results of OPC and MG8 after 28 days of curing, revealing distinct microstructural differences between the two binder systems. In terms of overall compactness, the MG8 demonstrates superior pore-filling capability. Compared to OPC, the porosity of MG8 is substantially reduced from 32.80% to 19.40%, accompanied by a decrease in cumulative pore volume from 0.23 mL/g to 0.13 mL/g in Figure 15a. These findings align well with its higher bulk density.



(**a**) Cumulative pore volume (**b**) Pore size distribution

Figure 15. MIP results of MG8 and OPC.

Table 4. Detailed pore characteristic parameters.

Sample	Actual Mercury Intrusion Volume (mL/g)	Porosity (%)	Bulk Density (g/mL)	Average Pore Diameter (nm)	Cumulative Pore Volume (mL/g)	Total Pore Surface Area (m^2/g)
OPC	0.23	33.3	1.4	34	0.22	27.2
MG8	0.13	19.1	1.5	72	0.13	6.9

Despite this enhanced densification, the evolution of pore size distribution differs fundamentally between the two materials. Pores can be classified into three categories according to different size ranges: micropores (<0.02 μm), mesopores (0.02–0.5 μm), and macropores (>0.5 μm) [66]. As shown in the incremental intrusion curves in Figure 15b, OPC exhibits a relatively broad pore size distribution, characterized by continuous and intense intrusion peaks across the micropore and mesopore ranges. This intensive distribution directly contributes to its high total pore surface area of 27.2 m^2/g. In contrast, the fine pore volume in MG8 is largely eliminated, replaced by a sharp, localized peak in the macropore region near 1 μm. This shifting of the pore size distribution effectively explains the seemingly contradictory observation: while the overall porosity of the geopolymer drops significantly, its average pore diameter actually exceeds that of OPC. Such a structural transition indicates that the abundant gel products generated during geopolymerization efficiently fill the finer capillary networks, reducing internal pore connectivity and ultimately yielding a much denser skeleton for the paste. The significant reduction in total pore surface area reported in Table 3 further corroborates this conclusion.

5. Conclusions

Based on comprehensive experimental evaluations of workability, mechanical properties, microstructural characteristics, and the crack repair efficacy of expansive agent-modified geopolymers, the following principal conclusions can be drawn.

(1) Although the incorporation of expansive agents inevitably consumes free water within the system, the effects of different expansive sources on the workability of geopolymer pastes vary significantly. In contrast to CaO and CSA, which induce severe flash setting and a precipitous decline in fluidity, the MgO-modified system provides an exceptionally broad operational window for early-stage crack repair. Concurrently, all three expansive agents effectively compensate for the drying shrinkage of the paste, with the MG8 formulation restricting the 28-day drying shrinkage rate to 0.23%.

(2) As the expansive agent dosage increases, the compressive strength of the modified geopolymers demonstrates a parabolic evolution trajectory characterized by an initial increase followed by a subsequent decline. Specifically, the 28-day compressive strength of the MG8 peaks at 44.10 MPa. In stark contrast to the CaO-modified group, which severely suppresses late-age strength evolution, the MgO-modified system preserves considerable potential for progressive strength development.

(3) In the grouting repair of concrete substrates featuring medium-to-wide cracks (2.0–3.0 mm), the MgO-modified geopolymer significantly outperforms traditional materials in restoring the load-bearing capacity of the damaged matrix. The flexible epoxy resin demonstrates unique advantages in enhancing interfacial tensile resistance. This is particularly evident in the remediation of 3.0 mm cracks, where the correspondingly increased resin volume yields a remarkable splitting tensile strength of 2.46 MPa.

(4) The MG8 repair system exhibits long-term durability significantly superior to that of conventional grouting materials under extreme exposure conditions, including sulfate

wetting–drying cycles, freeze–thaw cycles, and prolonged chloride/sulfate immersion. Specifically, this superior performance is characterized by robust volumetric stability under sulfate attack, as well as a tightly integrated crack interface that effectively impedes moisture migration, thereby averting structural degradation during cyclic freeze–thaw and dry–wet cycle.

(5) XRD, SEM, and MIP elucidate the dual mechanisms of the MgO-modified geopolymer. Intrinsically, the precipitation of micro-expansive $Mg(OH)_2$ at an optimal dosage effectively compensates for drying shrinkage; whereas excessive MgO content hinders the geopolymerization process. At the concrete repair interface, the MG8 system develops a highly compacted amorphous gel network (C-A-S-H/N-A-S-H). By densifying the pore structure and enhancing frictional interlocking, it achieves profound physical anchoring with the substrate.

The present study was conducted within a defined laboratory framework for the repair of 2–3 mm concrete cracks using the selected curing regime and injection procedure. The fresh-state characterization of the repair grouts was mainly based on flow spread and setting behavior, rather than on independent rheological parameters such as viscosity or yield stress. Therefore, the suitability of the proposed MG8 system is primarily demonstrated for injectable, non-structural cracks within the tested width range and under comparable curing conditions, while its direct applicability to sub-millimeter cracks, markedly different field curing environments, or elevated-temperature service conditions should be interpreted with caution. On this basis, subsequent work should further establish a more complete rheological description of the repair grout, verify the performance of MG8 under broader curing and service scenarios, and extend the evaluation from laboratory-scale material behavior to design-oriented and cost-performance considerations, so as to support a more comprehensive engineering assessment of the proposed repair system.

Author Contributions: Y.C.: Methodology, Investigation, Writing—original draft preparation. Z.L. (Zhiyuan Lu): Conceptualization, Methodology, Writing—review and editing. L.K.: Formal analysis, Resources, Funding acquisition. G.L.: Validation, Resources, Visualization. J.Y.: Conceptualization, Supervision, Writing—review and editing. S.L.: Investigation, Validation. G.W.: Investigation, Data curation, Writing—review and editing. J.X.: Formal analysis, Writing—review and editing. Z.L. (Zhengdong Luo): Conceptualization, Project administration, Funding acquisition, Supervision. All authors have read and agreed to the published version of the manuscript.

Funding: The authors acknowledge the project was supported by the Scientific Research Fund of the Hunan Provincial Education Department (Grant No. 25A0143) and the Yunnan Provincial Department of Education Scientific Research Fund (Grant No. 2026J1844).

Data Availability Statement: Data will be made available on request.

Conflicts of Interest: Author Linghai Kong and Genfu Liang were employed by the company The Third Engineering Co., Ltd. of CCCC Third Highway Engineering Bureau. Author Jianxin Yin was employed by the company CAMCE Engineering Co., Ltd. The remaining authors declare that the research was conducted in the absence of any commercial or financial relationships that could be construed as a potential conflict of interest.

References

1. Zhang, X.; Long, L.; Broere, W.; Bao, X. Smart sensing of concrete crack using distributed fiber optics sensors: Current advances and perspectives. *Case Stud. Constr. Mater.* **2025**, *22*, e04493. [CrossRef]
2. Howiacki, T.; Sieńko, R.; Bednarski, L. Structural concrete measurements: New distributed approach for standard specimens. *Measurement* **2024**, *235*, 115003. [CrossRef]
3. Wang, R.; Chen, R.; Yan, H.; Guo, X. Lightweight concrete crack recognition model based on improved MobileNetV3. *Sci. Rep.* **2025**, *15*, 15704. [CrossRef]

4. Alkannad, A.A.; Al Smadi, A.; Yang, S.; Al-Smadi, M.K.; Al-Makhlafi, M.; Feng, Z. Crack Vision: Effective concrete crack detection with deep learning and transfer learning. *IEEE Access* **2025**, *13*, 29554–29576. [CrossRef]
5. Zhang, J.; Qian, S.; Tan, C. Automated bridge surface crack detection and segmentation using computer vision-based deep learning model. *Eng. Appl. Artif. Intell.* **2022**, *115*, 105225. [CrossRef]
6. Shi, Y.; Wang, Y.; Wang, L.; Wang, W.; Yang, T. Bridge cable performance warning method based on temperature and displacement monitoring data. *Buildings* **2025**, *15*, 2342. [CrossRef]
7. Shi, Y.; Wang, Y.; Wang, L.; Wang, W.; Yang, T. Bridge tower warning method based on improved multi-rate fusion under strong wind action. *Buildings* **2025**, *15*, 2733. [CrossRef]
8. Wang, X.; Li, W.; Shen, M.; Wang, H. Numerical analysis of slurry-crack coupling in grouting repair process of multiple cracks in concrete material. *Materials* **2025**, *18*, 2472. [CrossRef]
9. Qin, S.; Wang, L.; Liu, J.; Xu, X.; Yu, F.; Wang, X. Interface bonding performance of magnetically driven epoxy-cement repair materials to repair concrete cracks in seawater environment. *Constr. Build. Mater.* **2025**, *498*, 144005. [CrossRef]
10. Roopa, A.K.; Ambale, D.; Hunashyal, A.M.; Patil, S. Synergistic effects of cementitious nanocomposites grouts fused with epoxy coatings for restoring concrete structures. *Sci. Rep.* **2025**, *15*, 40128. [CrossRef]
11. Jia, Q.; Li, J.; Wang, Y. Optimizing microbial grouting for vertical concrete crack sealing. *Results Eng.* **2025**, *26*, 105134. [CrossRef]
12. Aziz, T.; Haq, F.; Farid, A.; Cheng, L.; Chuah, L.F.; Bokhari, A.; Mubashir, M.; Tang, D.Y.Y.; Show, P.L. The epoxy resin system: Function and role of curing agents. *Carbon Lett.* **2024**, *34*, 477–494. [CrossRef]
13. Feng, Y.; Zhang, Z.; Yue, D.; Belko, V.O.; Maksimenko, S.A.; Deng, J.; Sun, Y.; Yang, Z.; Fu, Q.; Liu, B.; et al. Recent progress in degradation and recycling of epoxy resin. *J. Mater. Res. Technol.* **2024**, *32*, 2891–2912. [CrossRef]
14. Nguyen, H.A.Y.; Pham, D.H.; Ahn, Y.; Oo, B.L.; Lim, B.T.H. Machine learning and sustainable geopolymer materials: A systematic review. *Mater. Today Sustain.* **2025**, *30*, 101095. [CrossRef]
15. Xu, L.Y.; Lao, J.C.; Shi, D.D.; Cai, J.; Xie, T.X.; Huang, B.T. Recent advances in high-strength engineered geopolymer composites (HS-EGC): Bridging sustainable construction and resilient infrastructure. *Cem. Concr. Compos.* **2026**, *165*, 106307. [CrossRef]
16. Roviello, G.; Occhicone, A.; Gregorio, E.D.; Ricciotti, L.; Cioffi, R.; Ferone, C.; Tarallo, O. Geopolymer-based composite and hybrid materials: The synergistic interaction between components. *Sustain. Mater. Technol.* **2025**, *44*, e01404. [CrossRef]
17. Hamada, H.M.; Al-Attar, A.; Beddu, S.; Askar, M.K.; Yousif, S.T.; Majdi, A. Impact of rice husk ash on geopolymer concrete: A literature review and future directions. *Case Stud. Constr. Mater.* **2025**, *22*, e04476. [CrossRef]
18. Albidah, A.; Abadel, A.; Alrshoudi, F.; Altheeb, A.; Abbas, H.; Al-Salloum, Y. Bond strength between concrete substrate and metakaolin geopolymer repair mortars at ambient and elevated temperatures. *J. Mater. Res. Technol.* **2020**, *9*, 10732–10745. [CrossRef]
19. Girish, M.G.; Shetty, K.K.; Nayak, G. Thermal Characteristics of Fly Ash-Slag Based Geopolymer Concrete for Sustainable Road Construction in Tropical Region. *Int. J. Pavement Res. Technol.* **2026**, *19*, 834–862. [CrossRef]
20. Ye, H.; Radlińska, A. Shrinkage mechanisms of alkali-activated slag. *Cem. Concr. Res.* **2016**, *88*, 126–135. [CrossRef]
21. Özkılıç, Y.O.; Mohamud, M.A.; Yılmaz, F.; Alasiri, M.R.; Çelik, A.İ. The relationship of curing methods and curing temperatures with NaOH molarity and their effects on the behavior of geopolymer concrete. *Sci. Rep.* **2026**, *16*, 8346. [CrossRef]
22. Gomado, F.D.; Khalifeh, M.; Rafique, M. Harnessing waste glass as an expansive agent controller for enhanced geopolymer performance in oil and gas wells. *Geoenergy Sci. Eng.* **2024**, *243*, 213299. [CrossRef]
23. He, J.; Bai, W.; Zheng, W.; He, J.; Sang, G. Influence of hydrated lime on mechanical and shrinkage properties of alkali-activated slag cement. *Constr. Build. Mater.* **2021**, *289*, 123201. [CrossRef]
24. Jia, Z.; Yang, Y.; Yang, L.; Zhang, Y.; Sun, Z. Hydration products, internal relative humidity and drying shrinkage of alkali activated slag mortar with expansion agents. *Constr. Build. Mater.* **2018**, *158*, 198–207. [CrossRef]
25. Panchmatia, P.; Olvera, R.; Genedy, M.; Juenger, M.C.G.; Oort, E.V. Shrinkage behavior of Portland and geopolymer cements at elevated temperature and pressure. *J. Pet. Sci. Eng.* **2020**, *195*, 107884. [CrossRef]
26. Phoo-ngernkham, T.; Phiangphimai, C.; Intarabut, D.; Hanjitsuwan, S.; Damrongwiriyanupap, N.; Li, Y.; Chindaprasirt, P. Low cost and sustainable repair material made from alkali-activated high-calcium fly ash with calcium carbide residue. *Constr. Build. Mater.* **2020**, *247*, 118543. [CrossRef]
27. Zhang, J.; Wang, H.; Awed, A.M.; Xie, J.; Gu, F. Performance evaluation of high early strength micro-expansion geopolymer grout potentially used for sustainable road infrastructure. *Transp. Geotech.* **2024**, *49*, 101400. [CrossRef]
28. Alyousef, R.; Ebid, A.A.K.; Huseien, G.F.; Mohammadhosseini, H.; Alabduljabbar, H.; Ngian, S.P.; Mohamed, A.M. Effects of sulfate and sulfuric acid on efficiency of geopolymers as concrete repair materials. *Gels* **2022**, *8*, 53. [CrossRef] [PubMed]
29. Zheng, C.; Mao, Z.; Chen, L.; Qian, H.; Wang, J. Development of a novel rapid repairing agent for concrete based on GFRP waste powder/GGBS geopolymer mortars. *J. Build. Eng.* **2023**, *71*, 106542. [CrossRef]
30. Wang, K.; Lin, B.; Wu, B.; Yao, Y. Repair of ordinary concrete using basalt fiber reinforced geopolymer: High temperature resistance and micro-structure evolution of adhesive interface. *J. Build. Eng.* **2024**, *97*, 110712. [CrossRef]

31. Yao, N.; Chen, J.; Hu, N.; Ye, Y.; Xiao, Y.; Huang, Y. Experimental study on expansion mechanism and characteristics of expansive grout. *Constr. Build. Mater.* **2021**, *268*, 121574. [CrossRef]
32. Carballosa, P.; Calvo, J.L.G.; Revuelta, D.; Sánchez, J.J.; Gutiérrez, J.P. Influence of cement and expansive additive types in the performance of self-stressing and self-compacting concretes for structural elements. *Constr. Build. Mater.* **2015**, *93*, 223–229. [CrossRef]
33. Xiong, J.; Xie, J.; Zou, J.; Chen, Y.; Luo, Z. Research on the proportion optimization and working performance of environmental-friendly grouting repair material. *Met. Mine* **2026**, *2*, 313–320. (In Chinese)
34. *GB/T 8077–2023*; Methods for Testing Uniformity of Concrete Admixtures. Standards Press of China: Beijing, China, 2023.
35. *GB/T 1346–2024*; Test Methods for Water Requirement of Standard Consistency, Setting Time and Soundness of the Portland Cement. Standards Press of China: Beijing, China, 2024.
36. *JC/T 313–2009*; Test Method for Determining Expansive Ratio of Expansive Cement. Standards Press of China: Beijing, China, 2009.
37. *GB/T 17671–2021*; Test Method of Cement Mortar Strength. Standards Press of China: Beijing, China, 2021.
38. *GB/T 50081–2019*; Standard for Test Methods of Concrete Physical and Mechanical Properties. Standards Press of China: Beijing, China, 2019.
39. *GB/T 50082-2024*; Standard for Test Methods of Long-Term Performance and Durability of Concrete. Standards Press of China: Beijing, China, 2024.
40. Wen, X.; Zhan, Q.; Ye, H.; Xu, J.; Qian, B.; Luo, R.; Wu, X.; Liu, Z.; Fei, Z.; Guo, H. Synergistic surface plasmon resonance effect of Ag and S-scheme heterojunction in Ag/AgBr/$Bi_{24}O_{31}Cl_{10}$ towards enhanced enrofloxacin removal: Performance, degradation pathways and synergistic mechanism. *Environ. Res.* **2026**, *288*, 123249. [CrossRef]
41. Yu, N.; Zeng, X.; Ma, X.; Sun, Y.; Wang, Y.; Chen, B.; Luo, Z.; Dong, C.; Shen, K.; Wu, J. Preparation of Ce-Fe_2O_3/Al_2O_3 catalyst for simultaneous degradation of benzodiacetone and reduction of Cr(VI) by electro-Fenton process: Performance, mechanism, degradation pathways. *J. Alloys Compd.* **2025**, *1045*, 184745. [CrossRef]
42. Wang, L.; Zhang, J.; Sha, H.; Wang, Y.; Wang, H.; Zhu, G.; Lu, Y. Lanthanum-quaternized chitosan-modified zeolite for long-lasting operation of constructed wetland: A bifunctional strategy for simultaneous phosphorus removal and microbial clogging mitigation. *Water Res.* **2026**, *288*, 124688. [CrossRef]
43. Niu, M.; He, X.; Zhang, X.; Liu, Z.; Shen, Y.; Li, G. The coordination effect of expansive agent and fly ash on the hydration behavior and expansion performance of cement-based grouting materials. *Case Stud. Constr. Mater.* **2025**, *23*, e05067. [CrossRef]
44. Jia, Z.; Zhang, Z.; Jia, L.; Cao, R.; Yu, C.; Gao, Y.; Zhang, Y. Effect of different expansive agents on the early age structural build-up process of cement paste. *Cem. Concr. Compos.* **2023**, *144*, 105282. [CrossRef]
45. Park, S.; Lee, N.; Park, K.G. Early-age hydration behavior of calcium sulfoaluminate (CSA) cement/ordinary Portland cement-blended ultra-high performance concrete. *J. Build. Eng.* **2024**, *87*, 109058. [CrossRef]
46. Tong, L.; Li, F.; Wu, B.; Xu, C.; Lim, C.; Ding, H. Particle shape effect on creep and fluidity of granular packing. *J. Eng. Mech.* **2025**, *151*, 04025067. [CrossRef]
47. Zhang, Y.; Liu, X.; Wan, M.; Zhu, Y.; Zhang, K. Recent development of functional bio-based epoxy resins. *Molecules* **2024**, *29*, 4428. [CrossRef]
48. Li, L.; Shi, J.; Kou, J. Experimental study on mechanical properties of high-ductility concrete against combined sulfate attack and dry–wet cycles. *Materials* **2021**, *14*, 4035. [CrossRef]
49. Zhang, L.; Liu, H.; Wang, Z.; Sui, W.; Gong, Y.; Cui, J.; Ao, H.; Shang, L. Functional boron nitride/graphene oxide three-dimensional skeleton co-heat transfer epoxy resin composite. *J. Alloys Compd.* **2024**, *985*, 173935. [CrossRef]
50. Topark-Ngarm, P.; Chindaprasirt, P.; Sata, V. Setting time, strength, and bond of high-calcium fly ash geopolymer concrete. *J. Mater. Civ. Eng.* **2015**, *27*, 04014198. [CrossRef]
51. Bogas, J.A.; Brito, J.D.; Ramos, D. Freeze–thaw resistance of concrete produced with fine recycled concrete aggregates. *J. Clean. Prod.* **2016**, *115*, 294–306. [CrossRef]
52. Jin, F.L.; Li, X.; Park, S.J. Synthesis and application of epoxy resins: A review. *J. Ind. Eng. Chem.* **2015**, *29*, 1–11. [CrossRef]
53. Hu, Z.; Yang, Y.; Zhang, H. Durability and damage evolution of steel fiber and Nano-SiO_2 reinforced concrete under freeze-thaw and salt erosion environments based on acoustic emission and Computed Tomography analysis. *J. Build. Eng.* **2025**, *115*, 114595. [CrossRef]
54. Piasta, W. Analysis of carbonate and sulphate attack on concrete structures. *Eng. Fail. Anal.* **2017**, *79*, 606–614. [CrossRef]
55. Heshmati, M.; Sheikh, M.N.; Hadi, M.N.S. Development of sustainable fibre-reinforced self-compacting geopolymer concrete with enhanced resistance to chemical attacks and shrinkage. *Sustain. Mater. Technol.* **2026**, *47*, e01874. [CrossRef]
56. Gu, Z.; Dong, H.; Yuan, T.; Wang, Y.; Li, W.; Cao, Z.; Huang, T. Solidification/stabilization of mercury contaminated soil by geopolymer/MoS_2 composites. *J. Environ. Chem. Eng.* **2023**, *11*, 109546. [CrossRef]
57. Cui, Y.; Chen, S.; Li, L.; Wang, X.; Liu, J. Atomistic insights into the hydration behavior of N-A-S-H gel via Ca^{2+} substitution: A molecular dynamics simulation study. *J. Non-Cryst. Solids* **2026**, *673*, 123892. [CrossRef]

58. Zhang, J. Recent advance of MgO expansive agent in cement and concrete. *J. Build. Eng.* **2022**, *45*, 103633. [CrossRef]
59. Rashad, A.M. A concise on the effect of calcium oxide on the properties of alkali-activated materials: A manual for civil engineers. *Int. J. Concr. Struct. Mater.* **2023**, *17*, 72. [CrossRef]
60. Zhou, Z.; Chen, B. Effect of calcium sulphoaluminate cement on the early strength of one-part fly ash/slag-based geopolymers. *Eur. J. Environ. Civ. Eng.* **2026**, *30*, 1–22. [CrossRef]
61. Rajprasad, J.; Arunvivek, G.K.; Kumar, P.; Santhosh, G.; Gogineni, A.; Sembeta, R.Y. Interface improvement and multiscale assessment of recycled concrete aggregates with epoxy resin polymer. *Sci. Rep.* **2026**, *16*, 3697. [CrossRef] [PubMed]
62. Cao, F.; Miao, M.; Yan, P. Hydration characteristics and expansive mechanism of MgO expansive agents. *Constr. Build. Mater.* **2018**, *183*, 234–242. [CrossRef]
63. Guo, X.; Liao, L.; Xie, K.; Xu, W.; Lu, L.; Huang, K. Early-age mechanical and shrinkage performance of CaO-MgO expansive agent self-compacting concrete. *J. Build. Eng.* **2025**, *111*, 113165. [CrossRef]
64. Luo, B.; Su, Y.; Ding, X.; Chen, Y.; Liu, C. Modulation of initial CaO/Al_2O_3 and SiO_2/Al_2O_3 ratios on the properties of slag/fly ash-based geopolymer stabilized clay: Synergistic effects and stabilization mechanism. *Mater. Today Commun.* **2025**, *47*, 113295. [CrossRef]
65. Liu, Z.; Qi, X.; Ke, J.; Shui, Z. Enhancing the toughness of ultra-high performance concrete through improved fiber-matrix interface bonding. *Constr. Build. Mater.* **2025**, *491*, 142616. [CrossRef]
66. Zhang, S.; Ren, F.; Zhao, Y.; Qiu, J.; Guo, Z. The effect of stone waste on the properties of cemented paste backfill using alkali-activated slag as binder. *Constr. Build. Mater.* **2021**, *283*, 122686. [CrossRef]

Disclaimer/Publisher's Note: The statements, opinions and data contained in all publications are solely those of the individual author(s) and contributor(s) and not of MDPI and/or the editor(s). MDPI and/or the editor(s) disclaim responsibility for any injury to people or property resulting from any ideas, methods, instructions or products referred to in the content.